PAPER

Simple synthesis and characterization of vertically aligned $Ba_{0.7}Sr_{0.3}TiO_3$–$CoFe_2O_4$ multiferroic nanocomposites from $CoFe_2$ nanopillar arrays

To cite this article: Sergey Basov *et al* 2017 *Nanotechnology* **28** 475707

IOP Publishing Nanotechnology
Nanotechnology **28** (2017) 475707 (7pp) https://doi.org/10.1088/1361-6528/aa9016

Simple synthesis and characterization of vertically aligned $Ba_{0.7}Sr_{0.3}TiO_3$–$CoFe_2O_4$ multiferroic nanocomposites from $CoFe_2$ nanopillar arrays

Sergey Basov[1,3], Catherine Elissalde[1], Quentin Simon[1], Mario Maglione[1], Christopher Castro-Chavarria[1], Thomas Herrison de Beauvoir[1], Sandrine Payan[1], Kristiaan Temst[2], Vera Lazenka[2], Vlad Andrei Antohe[3], Pedro Miguel Pereira de Sá[3], David Sallagoity[1,3] and Luc Piraux[3]

[1] Institut de Chimie de la Matière Condensée de Bordeaux, Université de Bordeaux, UPR-CNRS 9048, Avenue du Docteur Schweitzer 87, F-33600 Pessac, France
[2] Instituut voor Kern- en Stralingsfysica, KU Leuven, Celestijnenlaan 200D, B-3001 Leuven, Belgium
[3] Institute of Condensed Matter and Nanosciences, Université catholique de Louvain, Place Croix du Sud 1, B-1348 Louvain-la-Neuve, Belgium

E-mail: luc.piraux@uclouvain.be

Received 28 July 2017, revised 12 September 2017
Accepted for publication 29 September 2017
Published 31 October 2017

Abstract

A new strategy to elaborate (1-3) type multiferroic nanocomposites with controlled dimensions and vertical alignment is presented. The process involves a supported nanoporous alumina layer as a template for growth of free-standing and vertically aligned $CoFe_2$ nanopillars using a room temperature pulsed electrodeposition process. $Ba_{0.70}Sr_{0.30}TiO_3$–$CoFe_2O_4$ multiferroic nanocomposites were grown through direct deposition of $Ba_{0.7}Sr_{0.3}TiO_3$ films by radio-frequency sputtering on the top surface of the pillar structure, with *in situ* simultaneous oxidation of $CoFe_2$ nanopillars. The vertically aligned multiferroic nanocomposites were characterized using various techniques for their structural and physical properties. The large interfacial area between the ferrimagnetic and ferroelectric phases leads to a magnetoelectric voltage coefficient as large as $\sim$320 mV cm^{-1} Oe^{-1} at room temperature, reaching the highest values reported so far for vertically architectured nanocomposite systems. This simple method has great potential for large-scale synthesis of many other hybrid vertically aligned multiferroic heterostructures.

Keywords: multiferroic, nanopillar, nanocomposite

(Some figures may appear in colour only in the online journal)

1. Introduction

Multiferroic nanostructured composites have attracted a lot of attention due to the control of the coupling between polarization and magnetization via strain [1–4] and their potential application in memory, actuators, sensors, and microwave devices [2, 5]. Intensive research in the field of multiferroic nanocomposites has opened new routes such as the fabrication of vertically aligned nanostructures, i.e. nanopillars embedded in a matrix, the so called (1-3) connectivity nanocomposite. These types of nanostructures offer the advantage to reduce the substrate imposed clamping effect, as compared to multilayered (2-2) types of multiferroic nanocomposites, and to enhance the interfacial area between the two phases, so that large magnetoelectric (ME) coupling can be expected [2, 6]. Up to now, vertically aligned multiferroic nanostructures from spinel and perovskite systems, including $CoFe_2O_4$–$BaTiO_3$ (CFO–BTO) and $CoFe_2O_4$–$BiFeO_3$ (CFO–BFO) were fabricated using pulsed laser deposition techniques [7, 8]. In order to control the long-range ordered vertical

interface, anodic aluminium oxide (AAO) membranes were used as a hard mask to grow columnar multiferroic nanocomposites [9]. Thick AAO membranes were also used as templates to fabricate multiferroic core–shell nanowire arrays using a combination of different synthesis processes, such as sol-gel processing, electrodeposition, and thermal annealing [10, 11]. However, to our best knowledge, there is no report on the fabrication of vertically aligned multiferroic nanocomposites based on a direct sputtering deposition of the ferroelectric film onto the top surface of the vertically aligned free-standing metallic nanopillar array structure grown by electrodeposition into AAO masks supported on silicon (Si) substrates.

In this work, we demonstrate a simple approach to synthesize vertically aligned $Ba_{0.7}Sr_{0.3}TiO_3$–$CoFe_2O_4$ (BSTO–CFO) nanocomposites with increased interfacial area between the ferroelectric and ferrimagnetic components. The $Ba_xSr_{1-x}TiO_3$ material is chosen due to the tunable Curie temperature (T_C), accompanied by the large dielectric permittivity through a variation of the $BaTiO_3/SrTiO_3$ composition, e.g. for the composition 70 at% Ba ($x \sim 0.7$) T_C is close to room temperature [12]. The fabrication process starts with the growth of free-standing and vertically aligned metallic $CoFe_2$ nanopillar arrays using pulsed electrochemical deposition inside nanopores of anodized AAO templates on Si substrates followed by a dissolution of the template. Then, BSTO–CFO film nanostructures are formed by direct deposition by radio frequency (rf) magnetron sputtering with Ar/O_2 reactive plasma of the BSTO matrix onto the $CoFe_2$ nanopillar arrays with *in situ* oxidation to form the desired oxidized CFO phase. This original *in situ* synthesis of vertically aligned multiferroic nanostructures allows us to improve the ordering of the magnetic nanopillars inside the matrix, and to preserve the nanopillar morphology. Indeed, when the oxidation of the free-standing $CoFe_2$ nanopillars was conducted by thermal treatment prior to BSTO deposition, a significant change of the surface roughness morphology of the pillars, and an increase of their diameter were found, thus preventing the penetration of BSTO through the ordered pillar arrays. We used different techniques to characterize the electrical and magnetic properties and to quantify the ME coefficient of the resulting BSTO–CFO multiferroic nanostructures.

2. Experimental details

High quality analytical grade (99.99%, unless otherwise specified) chemicals were used in this work as provided, without further purification. The aqueous solutions were prepared with ultra-pure deionized water purchased from VWR Chemicals, France. The close-packed array of the vertically aligned $CoFe_2$ nanopillars was produced by an electrochemical deposition within nanopores of the supported AAO template (figure 1), following a slightly modified protocol as previously reported [13, 14]. In brief, a freshly cleaned Si substrate was first prepared by depositing an ultra-compact Al film (~1 μm) over an intermediate Ti/Pt/Ti

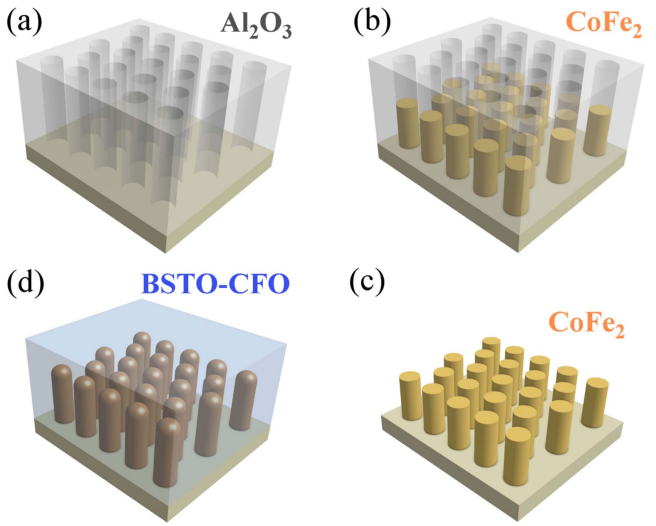

Figure 1. Sketch of the fabrication process of the vertically aligned BSTO–CFO nanostructures: (a) anodized AAO template supported on a Pt/Ti/Si substrate, (b) $CoFe_2$ nanopillars obtained by electrodeposition into the AAO nanoporous structure, (c) free-standing $CoFe_2$ nanopillar array obtained after chemical dissolution of the AAO template, (d) vertically aligned multiferroic BSTO–CFO nanostructures made by deposition of the BSTO layer onto the $CoFe_2$ pillar structure using rf magnetron sputtering with their simultaneous oxidation into a CFO nanopillar array.

under-layer (~5/50/5 nm), by magnetron sputtering (Plassys MP500S). Pt was used for a two-fold purpose: (1) to prevent nanopillar contamination via diffusion during the subsequent thermal treatment and (2) to serve as a bottom electrode for electrodeposition and physical measurements. The as-prepared Al/Ti/Pt/Ti/Si substrate was then exposed to a single step anodization process in 0.3 M oxalic acid ($H_2C_2O_4$) at 2 °C, by applying an anodic potential of 60 V from a Keithley 2400 sourcemeter during ~1000 s, the anodization process was stopped by the programme automatically after the current gradually increased and reached the set limit of 20 mA, which indicates that the alumina pores reached the conductive Pt layer. The anodization process was followed by a chemical widening of the nanopores in a 0.5 M sulphuric acid (H_2SO_4) solution (Merch, Germany) at 40 °C for 1 h. The resulting AAO film had a thickness of ~1.4 μm with a nanopore interspacing ~150 nm (the distance from centre to centre of nanopores) and an average pore diameter ~90 nm, generating a porosity factor $P \sim 35\%$ [15]. In the second stage, $CoFe_2$ alloy nanopillars were grown into the nanopores of the supported AAO template with a pulsed potentiostatic electrodeposition method. The $CoFe_2$ nanopillars were electrodeposited at ambient temperature from a single water-based electrolyte containing 0.1 M $CoSO_4 \cdot 7H_2O$ (98%, Alfa Aesar, Germany), 0.14 M $FeSO_4 \cdot 7H_2O$ (Merck, Germany), and 0.16 M H_3BO_3 (99.5%, Sigma-Aldrich, MO) in a standard three-electrode potentiostatic configuration using a PAR 263A Potentiostat/Galvanostat and a Pt foil as a counter electrode. The operating potential stepped from −1.5 V (versus Ag/AgCl reference electrode) during 20 ms and −0.5 V during 80 ms. The three-electrode setup includes (1) the Pt-coated Si substrate at the bottom of the pores serving as

a working electrode, (2) a Pt foil as counter electrode and (3) a Ag/AgCl reference electrode. The height of the nanopillars was easily controlled by varying the charge-controlled electrodeposition duration. The AAO template was then dissolved in 2 M of sodium hydroxide NaOH solution (Merck, Germany) during 20 min and washed in distilled water, thus leading to a free-standing and vertically aligned $CoFe_2$ nanopillar arrays on the Pt/Ti/Si substrate (figure 1(c)). Nanopillar arrays having an average height of ~200 nm were considered. The $Ba_{0.7}Sr_{0.3}TiO_3$ (BSTO) matrix was deposited by rf magnetron sputtering (Plassys MP700) in facing target configuration (90° off-axis geometry) using two home-made BSTO targets (rf power = 75 W) and reactive Ar/O_2 plasma (5 Pa and 1% O_2). Upon deposition, the substrates were kept at 650 °C with a substrate-to-target distance close to 40 mm. The deposition time was adjusted to fill the internal space of the pillar arrays as well as to obtain the desired BSTO layer thickness around 250 nm at the top of the nanopillar structure. Finally, Pt top electrodes having approximate diameters of 300 and 600 μm were deposited on the surface of the nanocomposites by rf magnetron sputtering through a shadow mask for the dielectric and ME characterizations.

Surface morphology was investigated using a high-resolution scanning electron microscopy JEOL 7600F (SEM) equipped with an energy dispersive x-ray (EDX) analyser. The crystal structure of the nanocomposites was characterized using a Bruker D8 Discover diffractometer in grazing incidence x-ray diffraction configuration (GIXRD), operating with CuKα radiation (CuKα_1 = 1.5406 Å, CuKα_2 = 1.5443 Å) and with an incident beam angle of 2°. Room temperature magnetic properties of the $CoFe_2$ and the BSTO–CFO nanostructures were investigated using an alternating gradient magnetometer (PMC MicroMag AGM) with a maximum magnetic field of ±14 kOe. The dielectric properties (capacitance and loss tangent) were measured as a function of temperature (from 80 to 400 K), frequency (from 100 Hz to 1 MHz), and bias voltage (with a maximum electric field ±5 V) using a HP 4194A impedance analyser. The effective permittivity of the deposits was calculated as

$$\varepsilon = \frac{C \times t}{\varepsilon_0 \times S}$$

using the measured capacitance value C, $\varepsilon_0 \approx 8.854 \times 10^{-12}\,\mathrm{F\,m^{-1}}$, the top Pt electrode surface area S, and the total thickness of the deposit t, assuming that the nanocomposite can be considered as a continuous material. The ME voltage coefficient was measured using an adjusted Quantum Design physical property measurement system (PPMS). The principles of ME voltage measurement were previously described in detail [16–18]. Briefly, the ac magnetic field (δH = 10 Oe) was generated at a fixed frequency of 1 kHz by sending an ac current (Keithley 6221) through a coil (1290 turns of AWG 36 phosphor bronze wire, with a diameter of 18 mm), which was assembled on the standard sample puck for PPMS electrical transport measurements. The ac voltage induced across the BSTO–CFO capacitor structure (δE) in response to a small ac magnetic field was measured with a lock-in amplifier (Stanford Research Systems, SR 830). Additionally, an ac magnetic field δH was superimposed onto the dc magnetic field H_{dc} (up to 4 Tesla) produced by the PPMS-internal superconducting magnet. Both the ac and dc magnetic fields were applied in out-of-plane direction (perpendicular to the nanostructure plane) and in the same direction as the measured ME voltage response δE. The ME coefficient was calculated using the relation

$$\alpha_E = \frac{\delta E}{\delta H} = \frac{\delta V}{t \times \delta H} = \frac{V_{ac}}{t \times H_{ac}},$$

where V_{ac} is the magnetically induced ac electric voltage across the sample, and t is the sample thickness.

3. Results and discussion

A tilted-view SEM image of the vertically aligned and free-standing $CoFe_2$ nanopillar arrays on Pt/Ti/Si substrate, obtained after removal of the AAO template, is shown in figure 2(a). The nanopillars height is ~200 nm and diameter ~90 nm, as expected from the morphological features of the porous AAO template. An average chemical analysis was provided by EDX (not shown) confirming a value of the Fe/Co ratio close to 2. Both ordering and uniformity in diameter of the $CoFe_2$ nanopillars can be seen on the top-view SEM image (figure 2(b)). A tilted-view SEM image (figure 2(c)) of the BSTO–CFO nanostructure shows that the BSTO matrix penetrates the spacing between the pillars to form the two-phase columnar structure made of the CFO pillars coated by the BSTO shells (schematically represented in figure 2(c)). A continuous BSTO layer of thickness ~250 nm is also formed at the top of the CFO nanopillars with a rather high surface roughness (figures 2(c) and (d)). The total thickness of the BSTO–CFO nanostructure is about 500 nm, which is larger than the sum of the $CoFe_2$ nanopillars height and the top BSTO layer thickness indicating the volume expansion of the nanopillars. Similar volume expansion was observed after the thermal treatment of the free-standing $CoFe_2$ nanopillar arrays.

The critical step to achieve BSTO–CFO nanostructure is clearly the *in situ* oxidation of the $CoFe_2$ metallic pillars during BSTO deposition. Both structural and magnetic characterization have been conducted to probe the oxidation efficiency of the nanopillar arrays. Figure 2(e) shows GIXRD patterns of the BSTO–CFO nanostructure, the $CoFe_2$ nanopillar arrays (JCPDS #48-1816), and the Pt/Ti/Si substrate annealed at ~600 °C (temperature selected close to the one used for the sputtering process). The oxidation of the $CoFe_2$ nanopillar array into a polycrystalline CFO nanopillar array during the BSTO matrix deposition was confirmed by XRD through the appearance of the CFO peaks (220), (311), and (444) (JCPD #22-1086). Note that the (222), (440) and (511) peaks are not visible because the phases corresponding to CFO and the annealed substrate can hardly be discriminated. The diffraction patterns of the BSTO–CFO nanostructure confirm the crystallization of the BSTO matrix with all peaks corresponding to the perovskite structure. Pt peaks and

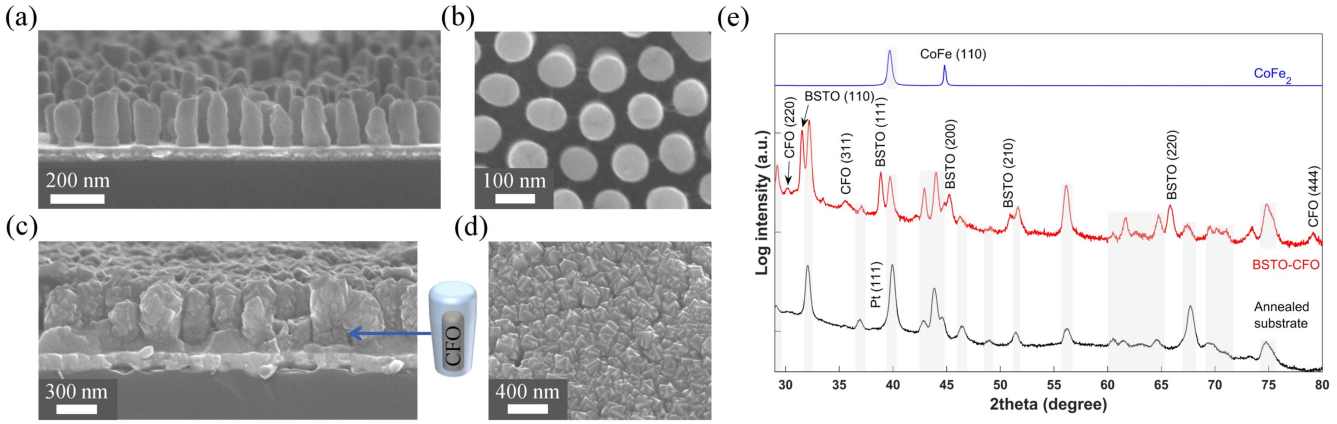

Figure 2. Tilted-view and top-view SEM images of a vertically aligned $CoFe_2$ nanopillar array (a), (b), SEM images of the samples corresponding to a tilted-view and a top-view on the BSTO–CFO nanostructure (c), (d). GIXRD patterns of the vertically aligned $CoFe_2$ nanopillar arrays (blue), the BSTO–CFO nanostructure (red), and the Pt/Ti/Si substrate annealed at ∼600 °C (black) (e).

additional peaks resulting from reactions and associated phase formation during annealing are observed in the XRD pattern of the Pt/Ti/Si substrate.

Figures 3(a) and (b) show the normalized magnetic hysteresis loops measured at room temperature with the field applied along the in-plane (perpendicular to pillar axis) and out-of-plane (parallel to pillar axis) directions. The effective magnetic anisotropy in a nanopillar array in the saturated state is determined by different contributions, namely shape anisotropy, dipolar inter-pillar coupling and magneto-crystalline anisotropy [19]. For the $CoFe_2$ nanowire array, the FD magnetocrystalline anisotropy can be neglected and the effective anisotropy is entirely magnetostatic, as pointed out previously [20]. Figure 3(a) reveals the easy axis of magnetization along the in-plane direction, as shape anisotropy, associated with the infinite array of the vertically aligned nanopillars behaving as a whole film, overcomes the uniaxial shape anisotropy along the out-of-plane direction of the individual nanopillars due to the high packing density and relatively small aspect ratio of the individual nanopillars [21]. In addition, this causes the coercivity $H_c \sim 190$ Oe and the remanence-saturation ratio ∼0.08 to become relatively small, irrespective of the direction of the applied field. Figure 3(b) shows the magnetic hysteresis curve for the embedded $CoFe_2O_4$ nanowire array in the BSTO matrix. The shapes of the hysteresis loops are similar in the in-plane and out-of-plane directions. This can be ascribed to the fact that the magneto-crystalline anisotropy energy dominates in the CFO nanopillar arrays, and there is no preferred crystallite orientation along the wire axes. Besides, large coercive field ($H_c \sim 1.7$ kOe) and remanence ($m/m_s \sim 0.44$) have been achieved in the BSTO–CFO multiferroic nanostructure. Such high coercive field is associated with the large magneto-crystalline anisotropy, and also possibly since the grain size is approaching the single-domain critical value [22]. The coercive fields for CFO nanowires are comparable to the room temperature values reported in the literature, thus confirming the efficacy of the *in situ* oxidation of the $CoFe_2$ nanopillars during the deposition of the BSTO matrix [22]. We also found that the experimentally measured magnetic moment of

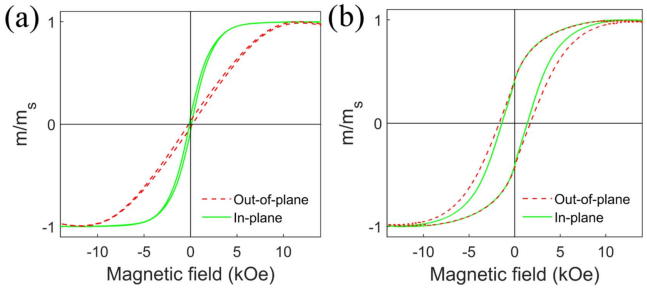

Figure 3. Room temperature hysteresis loops along in-plane (solid line) and out-of-plane (dashed line) directions for a vertically aligned $CoFe_2$ nanopillar array (a) and the BSTO–CFO multiferroic nanostructure (b). The magnetic moment is normalized to its value in the saturation state.

the metal nanopillar array decreased by a factor of 3.15 after the *in situ* oxidation. Taking into account the approximate oxidation-induced volume expansion (∼1.5) of the nanowires, this reduction of the sample's magnetic moment roughly corresponds to a large reduction in the saturation magnetization by a factor 4.7. This result is in good agreement with the expected ratio between the saturation magnetization for the $CoFe_2$ (∼1940 emu cm^{-3}) and CFO (∼400 emu cm^{-3}) bulk materials at room temperature [23, 24].

A macroscopic evidence of ferroelectricity is a prerequisite to expect ME coupling in such BSTO–CFO nanostructured composites. However, this remains challenging considering the complexity of these vertically aligned heterostructures. Dielectric investigations were performed, taking the well-behaved BSTO thin film as a reference for the BSTO–CFO nanostructures. Since the geometry of both sets of samples is quite different, only the capacitance and dielectric losses will be compared in the following.

Figure 4 shows the thermal variations at three frequencies (10 kHz, 100 kHz, and 1 MHz) of capacitance and dielectric losses for both a pure BSTO thin film (figures 4(c) and (b)) and the BSTO–CFO nanostructure (figures 4(a) and (b)). The pure BSTO thin film exhibits a broad $C(T)$ anomaly in a wide range of temperature, corresponding to a diffuse ferroelectric-

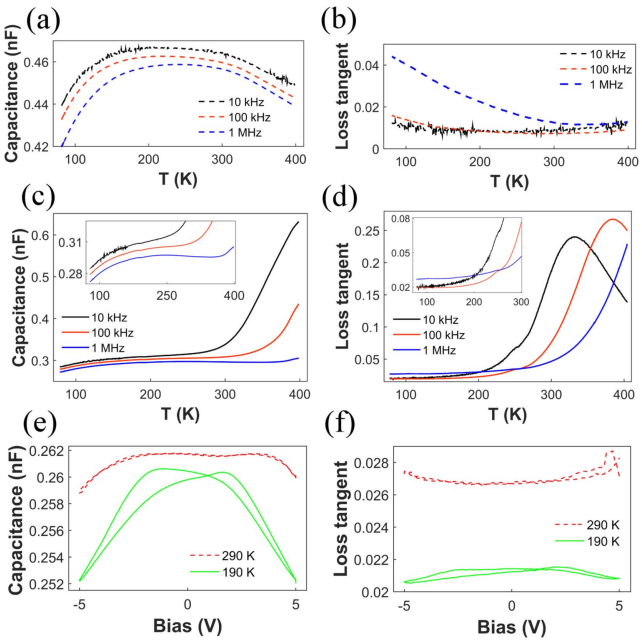

Figure 4. Capacitance and dielectric losses as a function of temperature for the BSTO thin film with thickness ∼250 nm (a) and (b) and the BSTO–CFO nanostructure capacitor (c) and (d), capacitance and dielectric losses (e) and (f) as a function of bias voltage for the BSTO–CFO nanostructure at two distinct temperatures, $T = 190$ K and $T = 290$ K.

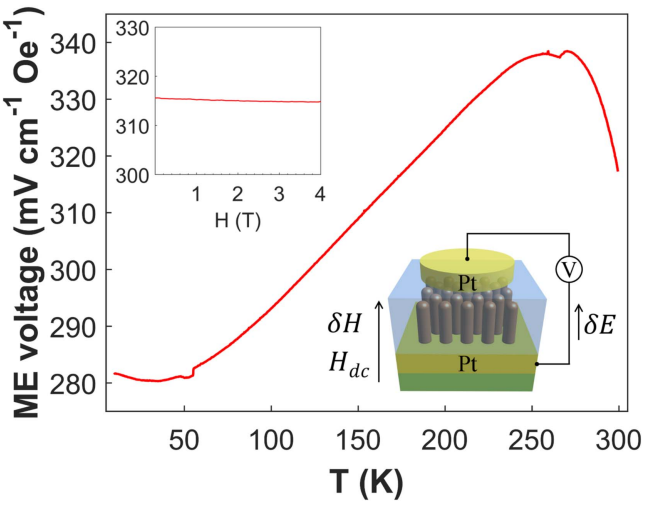

Figure 5. Temperature dependence of the ME voltage coefficient for the BSTO–CFO nanostructure. Schematic illustration of ME measurement and room-temperature variation with external dc magnetic field are shown in the bottom-right and top-left inset, respectively.

to-paraelectric transition (figure 4(a)). This diffuse behaviour is associated with a maximum of the capacitance occurring at lower temperature (250 K) compared to the ceramic counterpart ($T_C \sim 310$ K for the bulk $Ba_{0.7}Sr_{0.3}TiO_3$), as commonly observed for thin films [12, 25]. These discrepancies can arise from the microstructure of ferroelectric thin films including small grain size, residual strain and interfacial contributions [25, 26]. Therefore, the ferroelectric properties of the BSTO thin film are still partially present at room temperature. Over the whole temperature range, the dielectric losses of the BSTO thin film remain below ∼0.05 (figure 4(b)). For the BSTO–CFO nanostructure, the capacitance slightly increases when the temperature is raised from 80 to 200 K, similar to the pure BSTO thin film (see figure 4(c) and inset). However, the maximum in capacitance associated with the ferroelectric-to-paraelectric transition close to 250 K can only be observed at high frequency ∼1 MHz. At lower frequency this maximum is hindered by a strong increase of the apparent capacitance above 200 K. Accordingly, the dielectric losses showed pronounced peaks (figure 4(d)), whose maximum is shifted to higher temperature as the frequency increases. The relaxation follows an Arrhenius law with an activation energy E ∼0.45 eV, estimated from a fit over 30 frequencies in the range 1–200 kHz. This thermally activated relaxation process is responsible for an artificial increase of both the capacitance and losses at high temperature. This effect can be ascribed to conduction mechanism of the polycrystalline CFO phase due to electron hoping between multivalent cations like Fe and Co [27–29], for which an activation energy ∼0.4 eV is reported in the literature [27]. Another contribution can be related to charged defects inducing a Maxwell–Wagner type of interfacial polarization in agreement with Koop's two-layer model. Thus, the actual activation energy that we observed may result from several contributions including interactions among charged defects and interfacial accumulation of charges between BSTO and CFO due to the different types of charged defects in both phases. Without a deeper insight into the microscopic defects states, we cannot discuss further the activation energy value and compare it to the literature.

In the low temperature range ($T < 200$ K), for which the conductivity contribution can be neglected, the permittivity of the nanostructure ($\varepsilon \sim 50$) is lower than the one of the pure BSTO film ($\varepsilon \sim 150$) indicating the additional contribution of the low dielectric permittivity CFO phase.

In order to minimize the contribution at low frequency of space charge conductivity, ferroelectricity was probed by performing the capacitance–voltage (C–V) measurements at 1 MHz. The capacitance and dielectric losses measured at 190 K show two maxima with an opening of a hysteresis loop (figures 4(e) and (f)). In ferroelectric thin films, this is due to polarization reversal thus confirming the ferroelectric behaviour of our BSTO–CFO nanostructures. The same experiment performed at 290 K showed the progressive disappearance of the ferroelectric features and dominant paraelectric behaviour of the BSTO–CFO nanostructure in agreement with the diffuse ferroelectric–paraelectric transition around 250 K.

Direct measurement of the ME effect was performed to prove the ME nature of the vertically aligned BSTO–CFO nanostructures and to provide a macroscopic estimation of the ME coupling.

The temperature dependence of the ME voltage coefficient α_E in the range 10–300 K is shown in figure 5. The maximal value of the ME coefficient ∼340 mV cm^{-1} Oe^{-1} was observed around T ∼250 K. A decrease of the

temperature between 250 and 10 K leads to a reduction of the ME coefficient by ~17%. The shape of the $\alpha_E(T)$ curve can be ascribed to the temperature dependence of the dielectric and magnetic properties of the multiferroic nanocomposite. Since the Curie temperature for bulk CFO ($T_C \sim 790$ K) is much higher than room temperature, the peak in the curve can be associated with the ferroelectric–paraelectric transition of the $Ba_{0.7}Sr_{0.3}TiO_3$ phase around $T_C \sim 250$ K, as illustrated in figures 4(c) and (e). In previous works performed on PZT-$La_{0.7}M_{0.3}MnO_3$ (M = Sr, Ca) multilayers and the PZT-$La_{1.2}Sr_{1.8}Mn_2O_7$ thin films, the highest ME coefficient values were observed around the Curie temperature of the ferromagnetic phase [30, 31].

At room temperature, the ME voltage coefficient of the BSTO–CFO heterostructure displays very small variation (of the order of 1%) when an external dc magnetic field (up to 4 T) is superimposed on the time-varying field H_{ac}, as compared to the measured value in zero static magnetic field (see figure 5 (top-left inset)). The room temperature value of the ME voltage coefficient for the BSTO–CFO nanostructure (~320 mV cm^{-1} Oe^{-1}) is much higher than the values from macroscopic measurements reported earlier on (1-3) BFO-CFO composites [32–34], (in the range 20–74 mV cm^{-1} Oe^{-1}) and similar to that reported on (1-3) PZT-CFO composite (~390 mV cm^{-1} Oe^{-1}) [35]. It is further work to investigate the dependence of the ME properties of such vertically aligned multiferroic heterostructures on geometrical factors and material parameters.

4. Conclusions

In this work, we developed an original and efficient pathway for the synthesis of vertically aligned multiferroic nanocomposites. The method allowed the fabrication of regular, dense and free-standing $CoFe_2$ nanopillar arrays by electrodeposition through an AAO template supported on a Si substrate. Next, $Ba_{0.7}Sr_{0.3}TiO_3$–$CoFe_2O_4$ multiferroic nanostructures were grown through direct rf sputtering deposition of a ferroelectric film on the pillar structure, with *in situ* simultaneous oxidation of the ferromagnetic nanopillars, as confirmed by both structural and magnetic characterization. The synthesis approach preserves the morphology of the nanopillars during oxidation, improves the BSTO matrix penetration, and reduces the interface roughness between two constituents. The multiferroic nanostructures exhibit strain-mediated ME coupling, whose maximum ME coefficient was measured as ~340 mV cm^{-1} Oe^{-1} at around 250 K. Further optimisation of the fabrication process can be obtained by adjusting the magnetic packing fraction and pillar dimensions, thus opening a promising pathway towards versatile and controlled growth of vertically aligned multiferroic nanocomposites.

Acknowledgments

The IDS-FunMat European doctoral school is acknowledged for financial support. This work was partly supported by the Fédération Wallonie-Bruxelles (ARC 13/18-052, Supracryst) and by the Fonds de la Recherche Scientifique—FNRS under Grant no. T.0006.16. We are grateful to E Lebraud for grazing incidence x-ray diffraction measurements. Work at K U Leuven was supported by the Fund for Scientific Research —Flanders (FWO) and the K U Leuven Concerted Action (GOA/14/007).

ORCID iDs

Luc Piraux https://orcid.org/0000-0003-0684-4338

References

[1] Eerenstein W, Mathur N D and Scott J F 2006 Multiferroic and magnetoelectric materials *Nature* **442** 759–65
[2] Nan C-W, Bichurin M I, Dong S, Viehland D and Srinivasan G 2008 Multiferroic magnetoelectric composites: historical perspective, status, and future directions *J. Appl. Phys.* **103** 031101
[3] Fiebig M 2005 Revival of the magnetoelectric effect *J. Phys. D: Appl. Phys.* **38** R123–52
[4] Wang Y, Hu J, Lin Y and Nan C-W 2010 Multiferroic magnetoelectric composite nanostructures *NPG Asia Mater.* **2** 61–8
[5] Bibes M and Barthélémy A 2008 Towards a magnetoelectric memory *Nat. Mater.* **7** 425–6
[6] Bichurin M I, Petrov V M and Srinivasan G 2003 Theory of low-frequency magnetoelectric coupling in magnetostrictive-piezoelectric bilayers *Phys. Rev.* B **68** 054402
[7] Zheng H *et al* 2004 Multiferroic $BaTiO_3$–$CoFe_2O_4$ nanostructures *Science* **303** 661–3
[8] Zavaliche F *et al* 2005 Electric field-induced magnetization switching in epitaxial columnar nanostructures *Nano Lett.* **5** 1793–6
[9] Gao X, Rodriguez B J, Liu L, Birajdar B, Pantel D, Ziese M, Alexe M and Hesse D 2010 Microstructure and properties of well-ordered multiferroic $Pb(Zr,Ti)O_3/CoFe_2O_4$ nanocomposites *ACS Nano* **4** 1099–107
[10] Liu M, Li X, Imrane H, Chen Y, Goodrich T, Cai Z, Ziemer K S, Huang J Y and Sun N X 2007 Synthesis of ordered arrays of multiferroic $NiFe_2O_4$–$Pb(Zr_{0.52}Ti_{0.48})O_3$ core–shell nanowires *Appl. Phys. Lett.* **90** 152501
[11] Sallagoity D, Elissalde C, Majimel J, Maglione M, Antohe V A, Araujo F A, Pereira de Sá P M, Basov S and Piraux L 2016 Synthesis of dense arrays of multiferroic $CoFe_2O_4$–$PbZr_{0.52}Ti_{0.48}O_3$ core/shell nanocables *RSC Adv.* **6** 106716–22
[12] Parker C B, Maria J-P and Kingon A I 2002 Temperature and thickness dependent permittivity of $(Ba,Sr)TiO_3$ thin films *Appl. Phys. Lett.* **81** 340–2
[13] Mátéfi-Tempfli S, Mátéfi-Tempfli M and Piraux L 2009 Fabrication of nanowires and nanostructures: combining template synthesis with patterning methods *Appl. Phys.* A **96** 603–8
[14] Mátéfi-Tempfli S, Mátéfi-Tempfli M, Antohe V A and Piraux L 2009 Nanowires and nanostructures fabrication using template methods: a step forward to real devices combining

electrochemical synthesis with lithographic techniques *J. Mater. Sci., Mater. Electron.* **20** S249–54
[15] Nielsch K, Choi J, Schwirn K, Wehrspohn R B and Gösele U 2002 Self-ordering regimes of porous alumina: the 10 porosity rule *Nano Lett.* **2** 677–80
[16] Lazenka V V, Zhang G, Vanacken J, Makoed I I, Ravinski A F and Moshchalkov V V 2012 Structural transformation and magnetoelectric behaviour in $Bi_{1-x}Gd_xFeO_3$ multiferroics *J. Phys. D: Appl, Phys.* **45** 125002
[17] Dong S, Li J-F and Viehland D 2004 Characterization of magnetoelectric laminate composites operated in longitudinal-transverse and transverse-transverse modes *J. Appl. Phys.* **95** 2625–30
[18] Deng C, Zhang Y, Ma J, Lin Y and Nan C-W 2008 Magnetoelectric effect in multiferroic heteroepitaxial $BaTiO_3$–$NiFe_2O_4$ composite thin films *Acta Mater.* **56** 405–12
[19] Encinas-Oropesa A, Demand M, Piraux L, Huynen I and Ebels U 2001 Dipolar interactions in arrays of nickel nanowires studied by ferromagnetic resonance *Phys. Rev.* B **63** 104415
[20] Hua Z H, Chen R S, Li C L, Yang S G, Lu M, Gu B X and Du Y W 2007 $CoFe_2O_4$ nanowire arrays prepared by template-electrodeposition method and further oxidization *J. Alloy. Compd.* **427** 199–203
[21] Dmytriiev O *et al* 2013 Static and dynamic magnetic properties of densely packed magnetic nanowire arrays *Phys. Rev.* B **87** 174429
[22] Chinnasamy C N, Jeyadevan B, Shinoda K, Tohji K, Djayaprawira D J, Takahashi M, Joseyphus R J and Narayanasamy A 2003 Unusually high coercivity and critical single-domain size of nearly monodispersed $CoFe_2O_4$ nanoparticles *Appl. Phys. Lett.* **83** 2862–4
[23] Cullity B D and Graham C D 2009 *Introduction to Magnetic Materials* 2nd edn, ed L Hanzo (Hoboken, NJ: Wiley) pp 141–83
[24] Ojha S, Nunes W C, Aimon N M and Ross C A 2016 Magnetostatic interactions in self-assembled $Co_xNi_{1-x}Fe_2O_4$/$BiFeO_3$ multiferroic nanocomposites *ACS Nano* **10** 7657–64
[25] Tagantsev A K, Sherman V O, Astafiev K F, Venkatesh J and Setter N 2003 Ferroelectric materials for microwave tunable applications *J. Electroceram.* **11** 5–66
[26] Lobo R P S M, Mohallem N D S and Moreira R L 1995 Grain-size effects on diffuse phase transitions of sol-gel prepared barium titanate ceramics *J. Am. Ceram. Soc.* **78** 1343–6
[27] Jonker G H 1959 Analysis of the semiconducting properties of cobalt ferrite *J. Phys. Chem. Solids* **9** 165–75
[28] George M, Nair S S, Malini K A, Joy P A and Anantharaman M R 2007 Finite size effects on the electrical properties of sol–gel synthesized $CoFe_2O_4$ powders: deviation from Maxwell–Wagner theory and evidence of surface polarization effects *J. Phys. D: Appl. Phys.* **40** 1593–602
[29] Mahajan R P, Patankar K K, Kothale M B, Chaudhari S C, Mathe V L and Patil S A 2002 Magnetoelectric effect in cobalt ferrite-barium titanate composites and their electrical properties *Pramana* **58** 1115–24
[30] Srinivasan G, Rasmussen E T, Levin B J and Hayes R 2002 Magnetoelectric effects in bilayers and multilayers of magnetostrictive and piezoelectric perovskite oxides *Phys. Rev.* B **65** 134402
[31] Wu T, Zurbuchen M A, Saha S, Wang R-V, Streiffer S K and Mitchell J F 2006 Observation of magnetoelectric effect in epitaxial ferroelectric film/manganite crystal heterostructures *Phys. Rev.* B **73** 134416
[32] Yan L, Xing Z, Wang Z, Wang T, Lei G, Li J and Viehland D 2009 Direct measurement of magnetoelectric exchange in self-assembled epitaxial $BiFeO_3$–$CoFe_2O_4$ nanocomposite thin films *Appl. Phys. Lett.* **94** 192902
[33] Oh Y S, Crane S, Zheng H, Chu Y H, Ramesh R and Kim K H 2010 Quantitative determination of anisotropic magnetoelectric coupling in $BiFeO_3$–$CoFe_2O_4$ nanostructures *Appl. Phys. Lett.* **97** 052902
[34] Amrillah T *et al* 2017 Flexible multiferroic bulk heterojunction with giant magnetoelectric coupling via van der waals epitaxy *ACS Nano* **11** 6122–30
[35] Wan J-G, Weng Y, Wu Y, Li Z, Liu J-M and Wang G 2007 Controllable phase connectivity and magnetoelectric coupling behavior in $CoFe_2O_4$–$Pb(Zr,Ti)O_3$ nanostructured films *Nanotechnology* **18** 465708